Earth and Planetary Science Letters 597 (2022) 117819

Contents lists available at ScienceDirect

Earth and Planetary Science Letters

www.elsevier.com/locate/epsl

Fingerprinting secondary mantle plumes

Sierd Cloetingh [a,*], Alexander Koptev [b,c], Alessio Lavecchia [d], István János Kovács [e,f], Fred Beekman [a]

[a] Tectonics Research Group, Department of Earth Sciences, Utrecht University, Netherlands
[b] University of Tübingen, Department of Geosciences, Tübingen, Germany
[c] GFZ German Research Centre for Geosciences, Potsdam, Germany
[d] Istituto Nazionale di Geofisica e Vulcanologia, Bari, Italy
[e] MTA FI Lendület Pannon LitH2Oscope Research Group, Budapest, Hungary
[f] Institute of Earth Physics and Space Science ELKH, Sopron, Hungary

ARTICLE INFO

Article history:
Received 22 March 2022
Received in revised form 7 September 2022
Accepted 11 September 2022
Available online xxxx
Editor: J.P. Avouac

Keywords:
plume-lithosphere interaction
secondary plumes
hydrous plumes
lithosphere rheology
mantle transition zone
numerical modelling

ABSTRACT

Many vertical seismic velocity anomalies observed below different parts of the Eurasian plate are rooted in the transition zone between the upper and lower mantle (410–660 km), forming so-called secondary plumes. These anomalies are interpreted as the result of thermal effects of large-scale thermal upwelling (primary plume) in the lower mantle or deep dehydration of fluid-rich subducting oceanic plates. We present the results of thermo-mechanical numerical modelling to investigate the dynamics of such small-scale thermal and chemical (hydrous) anomalies rising from the lower part of the Earth's upper mantle. Our objective is to determine the conditions that allow thermo-chemical secondary plumes of moderate size (initial radius of 50 km) to penetrate the continental lithosphere, as often detected in seismo-tomographic studies. To this end, we examine the effect of the following parameters: (1) the compositional deficit of the plume density due to the presence of water and hydrous silicate melts, (2) the width of the weak zone in the overlying lithosphere formed because of plume-induced magmatic weakening and/or previous tectonic events, and (3) a tectonic regime varied from neutral to extensional. In our models, secondary plumes of purely thermal origin do not penetrate the overlying plate, but flatten at its base, forming "mushroom"-shaped structures at the level of the lithosphere-asthenosphere boundary. On the contrary, plumes with enhanced density contrast due to a chemical (hydrous) component are shown to be able to pass upwards through the lithospheric mantle to shallow depths near the Moho when (1) the compositional density contrast is $\geq$ 100 kg m^{-3} and (2) the width of the lithospheric weakness zone above the plume is $\geq$ 100 km. An extensional tectonic regime facilitates plume penetration into the lithosphere but is not mandatory. Our findings can explain observations that have long remained enigmatic, such as the "arrow"-shaped zone of low seismic velocities below the Tengchong volcano in south-western China and the columnar ("finger"-shaped) anomaly within the lithospheric mantle discovered more than two decades ago beneath the Eifel volcanic fields in north-western Germany. It appears that a chemical component is a characteristic feature not only of conventional hydrous plumes located over presently downgoing oceanic slabs, but also of upper mantle plumes in other tectonic settings.

1. Introduction

Traditionally, mantle plumes have been considered as thermal anomalies rising from the core-mantle boundary (CMB) throughout the entire Earth's mantle (Morgan, 1971). This concept has been confirmed by seismic tomography, which indicates vertically continuous low velocity anomalies interpreted as evidence for the formation of plumes in the lowermost mantle (Ritsema et al., 1999). The original finding that seismic heterogeneities in the mantle are mainly due to temperature contrasts was confirmed in several subsequent studies, which showed that an isochemical whole-mantle circulation can explain observed large-scale anomalies in global seismic tomography images without complications due to compositional variations (Schuberth et al., 2009; Maguire et al., 2016). This has inspired a first generation of numerical modelling studies

* Corresponding author.
E-mail address: S.A.P.L.Cloetingh@uu.nl (S. Cloetingh).

https://doi.org/10.1016/j.epsl.2022.117819

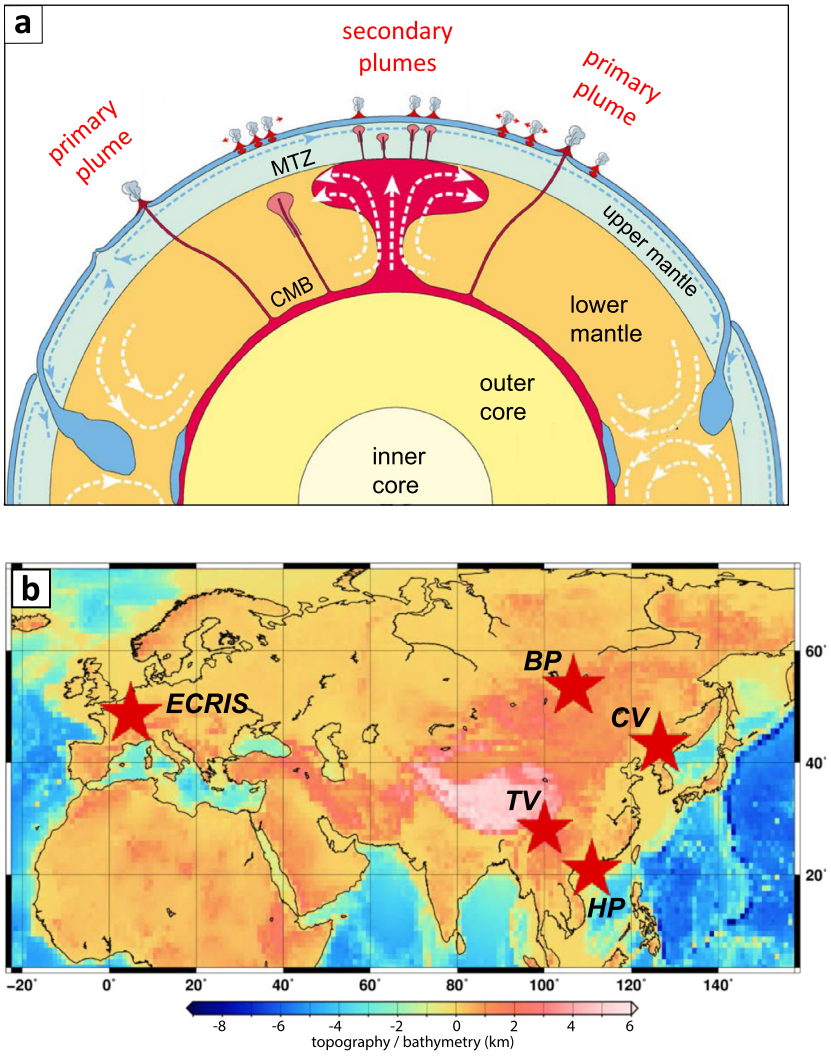

Fig. 1. a) A conceptual cross-section of the Earth's interior showing the different types of plumes: primary plumes originating in the CMB, and secondary plumes ascending through the upper mantle above primary superplumes stagnated below the MTZ (from Courtillot et al., 2003). b) Location of the secondary plumes in the Eurasian plate displayed in Fig. 2. Abbreviations: BP, Baikal plume; CV, Changbaishan volcano; ECRIS, European Cenozoic Rift System; HP, Hainan plume; TV, Tengchong volcano.

of plume-lithosphere interactions that consider plumes as purely thermal anomalies (Burov and Cloetingh, 2009).

Inconsistencies between the dimensions of plume tails in purely thermal mantle convection models (width not exceeding 400 km) and seismic tomography images showing wider (> 400 km) plume-like vertical channels (see Koppers et al., 2021, and references therein), led to interpretations invoking a thermo-chemical nature of plumes. Laboratory (Kumagai et al., 2008) and numerical (Dannberg and Sobolev, 2015) models have shown that thermo-chemical plume conduits are wider than purely thermal ones, suggesting that density heterogeneities in the mantle have a strong influence on mantle upwellings and alter plume characteristics. However, the chemical component could have two opposing effects on plume buoyancy. First, entrainment of deeply recycled subducted oceanic crust in the form of dense eclogite can result in higher density and thus lower compositional buoyancy in the plume material than in the surrounding peridotite (Sobolev et al., 2007). Consequently, less pronounced topographic uplift was predicted over such thermo-chemical plumes compared to their purely thermal counterparts (Sobolev et al., 2011). Second, water originating from stagnant slabs and stored in the upper-lower mantle transition zone (MTZ: 410-660 km; Helffrich and Wood, 2001) could give birth to hydrous plumes, positive chemical buoyancy anomalies that may rise to the Earth's surface even if the potential temperature of their source in the MTZ is within the range of the normal upper mantle temperature (Kuritani et al., 2011, 2019). The chemical component of plumes with a significant negative density contrast (up to -300 kg/m^3) that increases plume buoyancy has been extensively adopted in numerical models, especially in the context of plume-induced subduction initiation (Ueda et al., 2008; Gerya et al., 2015; Baes et al., 2016).

Early seismic tomography studies have already drawn attention to the fact that plumes are not always whole-mantle structures emanating from the CMB (superplumes) but may also be confined to the upper mantle (Ritsema et al., 1999). Such anomalies, which extend only across the upper mantle, have been classified as secondary plumes (Courtillot et al., 2003) and interpreted as the result of stagnation of the (primary) superplume at the base or within the MTZ (Fig. 1a). Regional and local seismic tomography studies have identified several examples of such secondary plumes (Fig. 1b; Fig. 2) in Europe (Granet et al., 1995; Sobolev et al., 1997; Plomerová et al., 2007) and in the East Asian region (Zhao et al., 2006; Lei et al., 2009a, 2009b; Tang et al., 2014; Xia et al., 2016), sometimes with extremely small horizontal extents of velocity anomalies of only ~100 km (Ritter et al., 2001). There are a number of fundamental questions about the dynam-

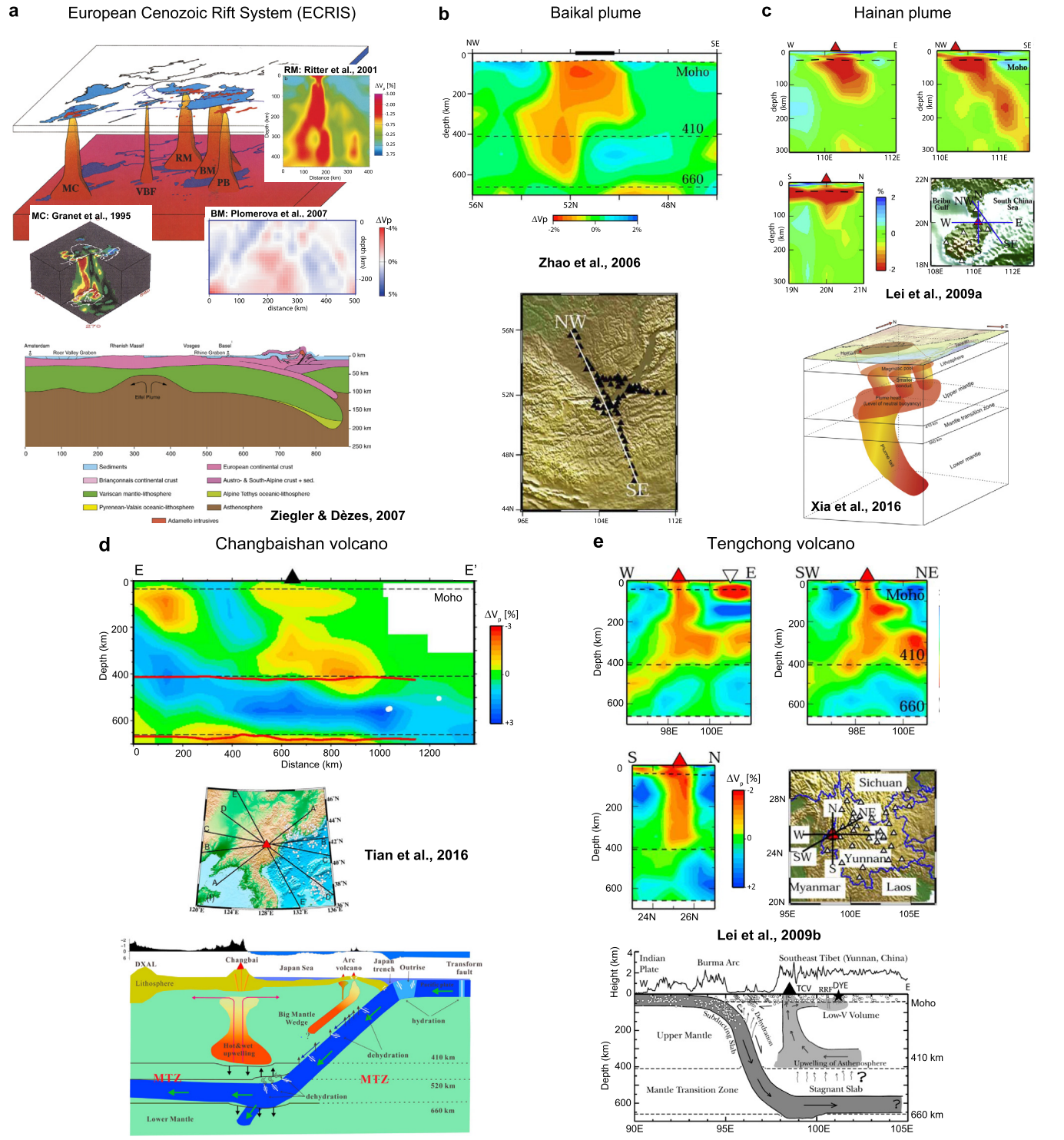

Fig. 2. Observations and conceptual interpretations of secondary plumes in different tectonic settings. a) European Cenozoic Rift System (ECRIS) plumes. Upper panel: Small-scale (baby) mantle plumes beneath different segments of the ECRIS (from Granet et al., 1995). Insets show seismic tomography images for the French Massif Central (from Granet et al., 1995), the Rhenish Massif/Eifel volcanic area (from Ritter et al., 2001), and the Bohemian Massif/Eger Graben (from Plomerová et al., 2007). Abbreviations: BM, Bohemian Massif; MC, Massif Central; PB, Pannonian Basin; RM, Rhenisch Massif; VBF, Vosges-Black Forest. The areas marked in red and blue are Tertiary-Quaternary volcanic fields and Variscan basement massifs, respectively. Lower panel: Schematic lithospheric transect across the Central Alps and the Rhenish Massif showing the tectonic position of the Eifel plume developed within a continental foreland on the subducting plate (from Ziegler and Dèzes, 2007). b) Baikal plume. Upper panel: Tomographic image beneath the Baikal rift with negative P-velocity anomalies (up to 2%) extending down to the MTZ. Lower panel: Location of tomographic cross-section (from Zhao et al., 2006). c) Hainan plume. Upper panel: Structure of the Hainan plume in the upper mantle shown by three cross-sections of P-wave velocity perturbations (from Lei et al., 2009a). Lower panel: Interpreted whole-mantle structure of the Hainan plume. Apart from a large segment extending from the CMB in the lower mantle, several much smaller patches are imaged from the MTZ to the LAB (from Xia et al., 2016). d) Changbaishan volcano. Top panel: Vertical cross-section (profile E-E' in middle panel) of P-wave tomography through the Changbaishan volcano. Middle panel: Location of all acquired profiles. Bottom panel: Cartoon showing the main features of the structure and dynamics of the upper mantle beneath the Changbaishan volcano (from Tian et al., 2016). e) Tengchong volcano. Top and middle panels: Structure of the upper mantle in the Tengchong volcano area shown by three cross-sections of seismic topography. Bottom panel: Schematic west-east vertical cross-section showing the upper mantle structure beneath the Indian plate, Burma Arc, and southeast Tibet (Yunnan, south-western China). Abbreviations: DYE, the 2003 Dayao earthquake zone; RRF, Red River fault; TCV, Tengchong volcano (from Lei et al., 2009b).

ics of these secondary plumes of modest size (sometimes referred to as baby plumes; see Koptev et al., 2021a) and their association with "finger"-shaped (narrow vertical tails) and "mushroom"-shaped (horizontally elongated heads) seismic anomalies detected not only in the sublithospheric upper mantle, but also inside the continental lithosphere overlying their source in the MTZ (Ritter, 2005; Zhao et al., 2011; Tian et al., 2016).

All previous numerical studies of thermo-chemical plumes have dealt with relatively large (» 100 km in resulting horizontal size of the head) mantle plume anomalies (Ueda et al., 2008; Baes et al., 2016). In contrast, a single systematic study of moderate size plumes has focused only on their thermal component (Koptev et al., 2021a). In this study, we present the results of numerical modelling that, for the first time, addresses small-scale plume anomalies of not only thermal but also chemical (hydrous) nature, with particular attention to the conditions required for their penetration into the overlying continental lithosphere.

2. Secondary plumes: observations and challenges in interpretation

2.1. Seismological observations and geodynamic settings

Numerous seismic velocity anomalies confined to the upper mantle (secondary plumes) have been reported for different regions of the Eurasian plate (Fig. 1b). They were originally discovered by detailed, specially developed seismological monitoring at regional and local scales in various branches of the European Cenozoic Rift System (ECRIS; Granet et al., 1995; Ritter et al., 2001; Ritter, 2005; Plomerová et al., 2007). Regional studies in the French Massif Central (Granet et al., 1995; Sobolev et al., 1997) and in the Eifel volcanic fields of north-western Germany (Ritter et al., 2001) provided evidence for a relatively shallow origin (near the MTZ) of these plumes since their tails extend only to a depth of 300-400 km. Moreover, in the western Bohemian Massif, a low velocity anomaly beneath the Tertiary Eger Rift system is restricted to a depth of only 250 km (Plomerová et al., 2007). Note, however, that the deepest fragments of the plume tails may not be visible in the seismic tomography data because of their narrow width. The small horizontal extent (∼100 km) of ECRIS plumes is sufficiently unique to warrant the introduction of a new term (baby plumes) to describe them (Koptev et al., 2021a). The European baby plumes can be viewed as an archetypal example of secondary plumes, originating from the same deep-sourced (super)plume which stagnates below or within the MTZ (Granet et al., 1995; Fig. 2a). The Baikal plume, delineated by a seismic velocity anomaly extending to a depth of ∼660 km (Zhao et al., 2006; Fig. 2b), is another example of a secondary plume developing in a continental rifting environment.

A columnar upwelling in the lower mantle beneath Hainan Island in southernmost China (Zhao, 2009) is interpreted as a return flow associated with deep subduction of the adjacent Pacific, Philippine Sea, and Indian slabs and their subsequent sinking down to the CMB (Zhao et al., 2011). This primary lower mantle plume accumulates at the level of the MTZ and further decomposes into smaller separate patches (Xia et al., 2016; Fig. 2c, lower panel), that are nearly identical to the pattern documented in the European region (Granet et al., 1995; Fig. 2a, upper panel).

In contrast to the traditional concept of secondary plumes originating from a primary source in the lower mantle (Courtillot et al., 2003; Fig. 1a), the prominent low velocity anomalies with a plume-like shape are also observed in upper mantle that is separated from the lower mantle by stagnant slabs at the MTZ (Fig. 2d-e). These seismic anomalies and the associated intraplate magmatism – the Changbaishan volcanic field on the China-North Korea border (Tian et al., 2016; Fig. 2d) and the Tengchong volcano in south-western China (Lei et al., 2009b; Fig. 2e) – are related to the combined effect of large-scale return flow in response to subduction (Zhao et al., 2009) and deep dehydration of the Pacific and Indian (Burma) slabs stagnating in the lower part of the MTZ (Kuritani et al., 2019) due to the jump in viscosity at 660 km (Forte and Mitrovica, 1996). It is important to note that the East Asian plumes originate in the big mantle wedge (Zhao et al., 2009) between the stagnant slabs and the overriding lithosphere (Fig. 2d-e, bottom panels), whereas the European baby plumes develop in a continental foreland setting on top of the subducting plate (Ziegler and Dèzes, 2007; Fig. 2a, lower panel). This suggests that emplacement of secondary plumes could occur in a broad spectrum of possible geodynamic environments across the subduction zone from foreland (Europe) to hinterland (China).

A striking feature of many of these secondary plumes is that they not only rise from the MTZ to the bottom of the lithosphere (or lithosphere-asthenosphere boundary; LAB), forming tilted (Hainan plume; Fig. 2c) or vertical (Tengchong plume; Fig. 2e) anomalies in the sublithospheric upper mantle (Lei et al., 2009a, 2009b), but also penetrate further into the overlying plate and produce intra-lithospheric "finger"-like structures (see, e.g., the Eifel plume in the inset from Ritter et al., 2001 in Fig. 2a). Furthermore, this vertical penetration up to the surface could also be accompanied by horizontal flow leading to the formation of "mushroom"-like structures within the lithosphere, as in the case of the Changbaishan plume (Tian et al., 2016; Fig. 2d, top panel). These intra-lithospheric "mushrooms" should not be confused with the "pancakes" or "mushrooms" that result from flattening of the plume head below the LAB, as commonly assumed in conceptual considerations and modelling studies.

2.2. Constraints from experimental petrology and geochemistry

Volatiles, especially water, play a fundamental role in determining the physical properties of the Earth's upper mantle. It is well known that the incorporation of water into nominally anhydrous minerals (e.g., olivine and wadsleyite) reduces their density and effective viscosity (e.g., Karato et al., 2006; Richard and Bercovici, 2009). Water enrichment also affects seismic wave velocities of these minerals (Wang et al., 2019). The shift of the solidus curve to greater depths due to the presence of fluids results in a higher degree of partial melting (e.g., Ohtani, 2020). Because hydrous silicate melts are also much lighter and less viscous than the surrounding environment (Drewitt et al., 2022), their presence further increases the buoyancy of rocks undergoing hydration (e.g., Matsukage et al., 2005; Hack and Thompson, 2011) and abruptly decreases the seismic velocities (Gerya et al., 2006). As a result, even relatively small structures such as secondary plumes can be detected in seismotomographic images (see section 2.1).

The best-known example of the effects of rock hydration and associated partial melting on rock buoyancy is the development of so-called cold plumes (Ghosh et al., 2020), which form above a subducting plate at relatively shallow depths of up to ∼150 km as a result of the infiltration of slab-derived water-rich fluids into the mantle wedge (Gerya et al., 2006). Further subduction of the oceanic plate, which consists of serpentinites, hydrated sediments, carbonates, and carbonated basalts (Safonova et al., 2015), is often followed by stagnation at the level of the MTZ (Fukao et al., 2009). As mentioned above (see section 2.1), dehydration of the fluid-rich stagnant slab leads to upwelling of wet and therefore buoyant mantle material in the form of atypical (i.e., not connected to the lower mantle) secondary plumes, which are visible in seismic tomography and expressed at the surface in intraplate volcanic fields such as Changbaishan (Tian et al., 2016; Fig. 2d) and Tengchong (Lei et al., 2009b; Fig. 2e). Over geological times, continuous subduction and subsequent stagnation of oceanic slabs causes the

accumulation of fluids in the MTZ, which is known to be a vast potential reservoir of water in the deep Earth, with concentrations reaching up to 1 wt%, as demonstrated experimentally and by geophysical methods (e.g., Freitas et al., 2017). Importantly, the large water content in the MTZ is not restricted to zones of current or recently subducted slabs. Hydration of the MTZ beneath cratons in southern Africa, for example, is attributed to subduction processes in the Precambrian (Blum and Shen, 2004). Furthermore, a recent study by Zhou et al. (2022) shows only minor differences (much smaller than the standard statistical deviation) in estimated water content within different segments of the MTZ in various tectonic settings. These findings can lead to far-reaching inferences about the ubiquitous hydration of the MTZ. Therefore, any primary plume, that inevitably traverses this water-rich layer between the upper and lower mantle on its way from the CMB to the Earth's surface, can incorporate fluid-enriched components in the resulting volcanism. Indeed, the ratios of hydrogen isotopes and diagnostic trace elements, as well as the water content of associated primitive mafic melts, point to a hydrous mantle source, for example, in the picrites of the Emeishan Large Igneous Province (Liu et al., 2022). These hydrous components are also found in European magmatic centres (Gu et al., 2018; Kovács et al., 2020) related to secondary baby plumes (Koptev et al., 2021a) and, naturally, in East Asian volcanoes associated with plumes developed in the big mantle wedge above slabs that are currently stagnating at the MTZ (Kuritani et al., 2019). However, distinguishing between purely thermal and hydrous plumes based solely on geochemical signatures is not trivial because the latter are also usually accompanied by a temperature anomaly. Accordingly, even apparently purely hydrous secondary plumes in the East Asian region, which are formed without any connection to hot upwellings in the lower mantle, may be heated by U-Th-K-enriched continental material tectonically eroded from the overriding plate and accumulated together with oceanic slabs in the MTZ (Safonova et al., 2015). Therefore, both hydrous and thermal components should always be jointly considered in the context of a secondary plume.

Despite advances in theoretical (Hack and Thompson, 2011) and experimental (Matsukage et al., 2005) studies, quantitative estimates of the effects of water on the density and deformation of solid rocks and hydrous silicate melts remain a complex issue (e.g., Gaillard et al., 2019). In the absence of a robust parameterization, we test in our modelling study a very wide range of the hydrous component of the plume, implemented in terms of various chemical densities, in combination with a moderate thermal component, which is always present but remains the same in all experiments. In this way, we explore different types of secondary plumes, from purely thermal to strongly hydrous, also in the context of variations in the structuring of the overlying lithosphere (weak zones of different widths) and tectonic conditions (from neutral to far-field extension). By varying these controlling parameters, we search for modelling settings that allow us to reproduce observed features such as the enigmatic "finger"-like penetration of plume material into the lithosphere (Ritter et al., 2001).

3. Modelling approach

We have modelled the process of interaction between the small-scale mantle plume rising from the MTZ and the rheologically stratified continental lithosphere, with particular attention to how this thermo-chemical anomaly settles at the LAB and subsequently penetrates to shallower depths in the lithospheric mantle. We performed the simulations using the open-source code ASPECT 2.3.0 (Kronbichler et al., 2012), which is specifically developed to solve geodynamic problems related to mantle convection, taking into account the motion and deformation of highly viscous materials with complex nonlinear rheology (see Methods in Appendix A for more details).

3.1. Model design

The model encompasses a rectangular area with a horizontal extent (W) of 800 km and a vertical thickness (H) of 400 km. The spatial resolution is 2.5 km in both the horizontal and vertical directions. The model comprises a three-layered continental lithosphere overlying a sublithospheric mantle (H_{SM} = 280 km). A 120-km-thick plate contains a crust evenly divided into upper (H_{UC} = 17.5 km; wet quartzite) and lower (H_{LC} = 17.5 km; dry diabase) parts, and a lithospheric mantle (H_{LM} = 85 km; dry olivine), consistent with observations of a partially thinned continental lithosphere in Central Europe (e.g., Ziegler and Dèzes, 2007) and East Asia (e.g., Kuritani et al., 2019). At the base of the model, a small-scale thermo-chemical anomaly (mantle plume) is seeded at the onset of the simulations as a semi-circle with a radius (R) of 50 km (Fig. 3a). Note that in contrast to Koptev et al. (2021a), who focused mainly on the consequences of the effects of the small thermal anomalies already placed below the bottom of the lithosphere, in this study we also include the upwelling phase from the lower part of the sublithospheric upper mantle.

The initial geotherm is piece-wise linear for the crustal and lithospheric domains (Fig. 3b), with given temperatures at the upper boundary of the model (surface temperature: T_0 = 0 °C), at the base of the crust (Moho temperature: T_M = 600 °C), and at the base of the lithospheric mantle (LAB temperature: T_{LAB} = 1300 °C). The rheological structure of the lithosphere resulting from such a compositional and temperature setting is characterized by a vertical alternation of brittle and ductile rock behaviour (Fig. 3c). Temperatures in the sublithospheric mantle follow a nonlinear adiabatic law: $T(z) = T_P exp\left(\frac{\alpha g z}{C_P}\right)$ with the potential temperature of the mantle (T_P) of 1280 °C (see Appendix A for definition and values of other parameters). The adiabatic temperature at the base of the model box (T_B) gives the value of 1425 °C (Fig. 3b). The mantle plume is implemented in the model as a thermal anomaly with higher temperatures than the surrounding upper mantle, obtained by adding a temperature term (ΔT = 150 °C) to an adiabatic thermal gradient (Fig. 3b). The temperatures at the top (T_0 = 0 °C) and bottom (T_B = 1425 °C) of the model are constant throughout the temporal evolution of the system. As for the thermal boundary conditions at the vertical (right and left) boundaries, we consider them to be insulating and apply a zero conductive heat flux there.

As mentioned above, the secondary mantle plumes derived from the MTZ may be enriched with fluids and partially molten. These two factors result in an increased compositional (chemical) buoyancy relative to the surrounding mantle (e.g., Kuritani et al., 2019, and references therein). Previous studies have shown that the compositional deficit of the plume density can significantly affect the nature of plume-lithosphere interactions (e.g., Baes et al., 2016). To test the impact of different concentrations of the hydrous component (and thus potentially different degrees of resulting partial melting), we follow the approach of Baes et al. (2016) and conduct experiments in which the compositional contrast between the reference densities of the surrounding mantle and the plume ($\Delta\rho_0$) varies in the range from 0 to 300 kg m^{-3}. This chemical density contrast is superimposed on the thermal buoyancy due to excess temperature. For a given ΔT of 150 °C, the thermal density contrast at the beginning of the model is ~15 kg m^{-3}. Note that unlike the compositional density deficit, which remains the same throughout the evolution of the model, the thermal buoyancy is defined by the current temperature difference and is therefore updated at each time step. As a result, it can change significantly over time, depending, for example, on the rate of plume migration.

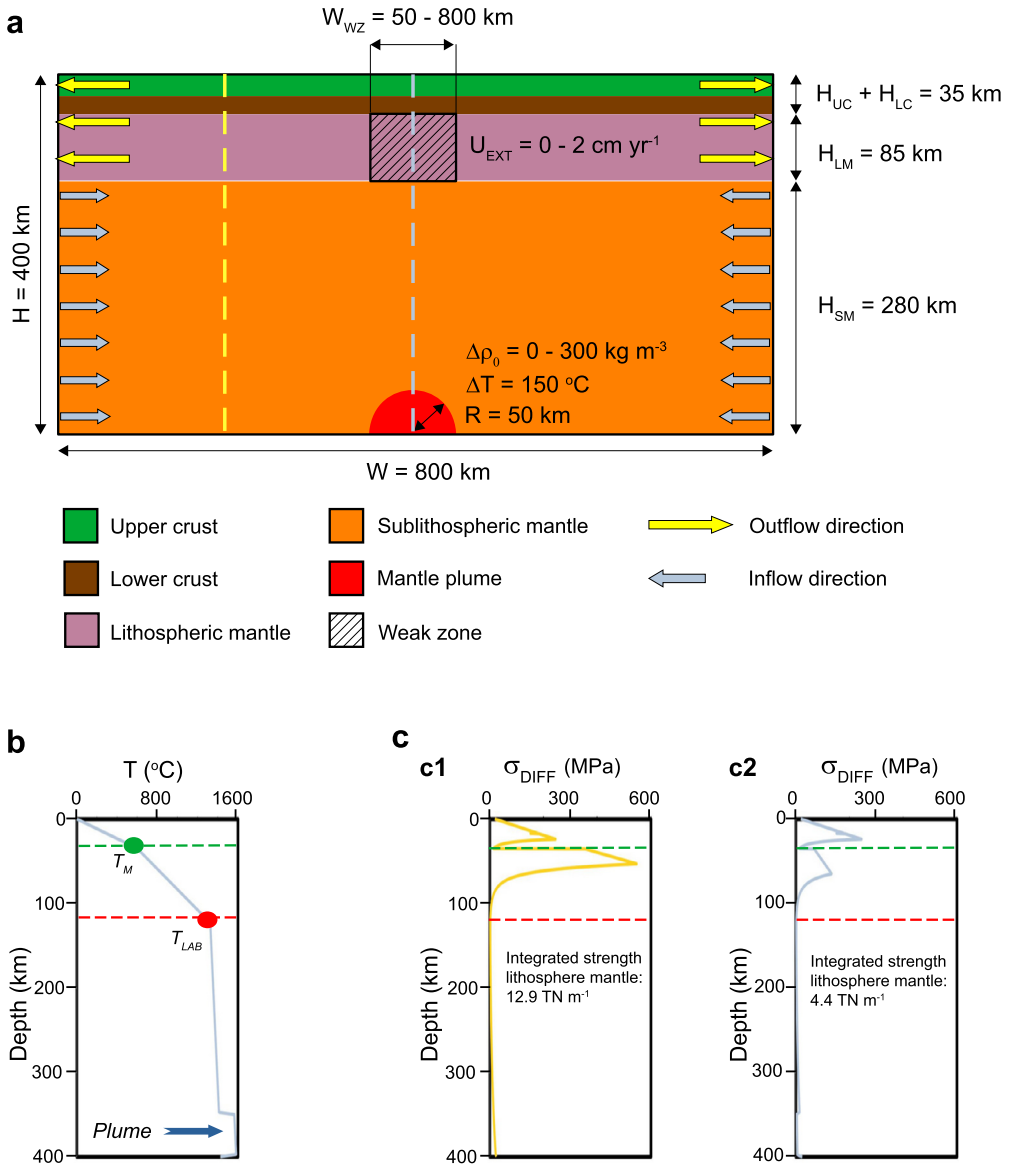

Fig. 3. Model setup. a) Material layout and velocity boundary conditions. The weak lithospheric zone of varying width is located directly above the semi-circular thermo-chemical (hydrous) plume, which is seeded at the bottom of the model at a depth roughly corresponding to the upper boundary of the MTZ. The outflow of lithospheric material due to tectonic extension is balanced by an equal and opposite inflow into the sublithospheric mantle. b) Vertical profile of initial temperature. The piece-wise linear distribution in the lithospheric domain is defined by the given temperatures at the Moho (T_M) and LAB (T_{LAB}). c) Vertical profiles of differential stresses (σ_{DIFF}) calculated for the initial temperature distribution (see panel b) and a constant strain rate of 10^{-15} s^{-1} for the model segments corresponding to the normal (panel c1) and weak (panel c2) lithosphere (the location of the profiles is indicated in panel a). The green and red horizontal dashed lines refer to the Moho and LAB, respectively. Note the significantly reduced brittle component in the weakened lithospheric mantle, resulting in a strong contrast in the integrated lithospheric strength values.

Another effect of the fluids and melts in the plume is that they can significantly alter the mechanical properties of the rocks (Gerya et al., 2015; Lavecchia et al., 2017). Once a partially molten body of the mantle plume reaches the LAB, buoyant and low-viscosity melts (e.g., Dingwell, 1995) penetrate the lithosphere at an upward velocity that is much faster compared to the rate of rock deformation (e.g., Hawkesworth et al., 1997), leading to quasi-instantaneous rheological weakening of the overlying lithospheric segment, which is subjected to melt percolation (Gerya et al., 2015). Previous studies have shown that melt-induced reduction in lithospheric strength plays an important role for geodynamic processes in both oceanic (Ueda et al., 2008; Baes et al., 2020) and continental (Lavecchia et al., 2017; Koptev et al., 2021b) environments. Although the melting process and subsequent percolation of the melt through the solid rock matrix are not directly modelled in our study, we account for the effects of magmatic weakening in an implicit manner by implementing a weak zone in the lithosphere located directly above the plume (Fig. 3a). This zone of weakness is characterized by significantly lower values of brittle rheological parameters (see Table A.2 in Appendix A), resulting in a decrease in the strength of the lithospheric mantle by ~400 MPa (cf. Figs. 3c1 and 3c2), consistent with values reported by Rosenberg and Handy (2005) for rocks with melt fractions less than 7% vol. Importantly, the lateral variations in the calculated integrated strength of the lithosphere (~8.5 TN m^{-1}; Fig. 3c) are close to the estimate of the strength contrast between an ancient craton and a continental rift zone (~8.9 TN m^{-1}; Glerum et al., 2020). The horizontal extent (or width) of the weak zone (W_{WZ}) ranges from 50 km (corresponding to the approximate lateral size of the plume head at the time of emplacement beneath the lithosphere; see modelling results) to 800 km (i.e., including the entire overlying lithosphere) in the various experiments. Note that the

Table 1
Parameters defining composition field, initial temperature distribution, and velocity boundary conditions.

Parameter	Symbol	Value
Model width	W	800 km
Model depth	H	400 km
Thickness of the upper crust	H_{UC}	17.5 km
Thickness of the lower crust	H_{LC}	17.5 km
Thickness of the lithospheric mantle	H_{LM}	85 km
Thickness of the sublithospheric mantle	H_{SM}	280 km
Surface temperature	T_0	0 °C
Moho temperature	T_M	600 °C
LAB temperature	T_{LAB}	1300 °C
Mantle potential temperature	T_P	1280 °C
Model base temperature	T_B	1425 °C
Plume radius	R	50 km
Plume excess temperature	ΔT	150 °C
Compositional deficit of the plume density	$\Delta\rho_0$	0 – 300 kg m^{-3}
Width of the weak zone in the lithosphere	W_{WZ}	50 – 800 km
Rate of tectonic extension	U_{EXT}	0 – 2.0 cm yr^{-1}

end member with the completely weak lithospheric mantle (W_{WZ} = 800 km) is not typical of present-day conditions on Earth and that this scenario is more conceivable for the hotter and more vigorously convecting early Earth, which produces hotter thermal instabilities in the upper mantle with a higher degree of partial melting (Ueda et al., 2008).

The mechanical boundary conditions include free slip (horizontal) at the base of the model domain, while a free surface is assumed for the upper boundary. In most experiments, free slip (vertical) is also adopted at the left and right edges of the model. However, because the stress state of the lithosphere can affect the penetration of small-scale plumes to shallow depths (Koptev et al., 2021a), in some simulations we impose a horizontal extensional velocity (U_{EXT} in the range from 0.25 to 2.0 cm yr^{-1}) at the lateral boundaries of the lithosphere for a depth interval of 0–120 km, while a compensating flow in the opposite direction is applied in the sublithospheric part of the model box (Fig. 3a). Since the zones of elevated LAB are known to serve as sinks for a buoyant mantle plume (Sleep, 1996), we exclude thinning of the lithosphere before it begins to interact with the mantle plume. To this end, far-field extension is not applied at the onset of the simulation, but only when the top of the plume head reaches a vertical distance of ≈50 km from the base of the lithosphere. As a result, plume-lithosphere interaction is assisted by tectonic extension, but the overlying plate is not subjected to localized deformation prior to plume emplacement at its bottom. The series of experiments with nonzero tectonic extension (U_{EXT} > 0 cm yr^{-1}) allows us to examine the combined effect of plume erosion and tectonic thinning of the lithosphere in the context of a mixed mechanism of active-passive rifting (Koptev et al., 2015, 2018).

The parameters characterizing the model geometry, initial temperature distribution, and velocity boundary conditions are summarized in Table 1 while the detailed description and assumed values for the thermal and rheological parameters can be found in Tables A.1–A.3 in Appendix A.

3.2. Modelling procedure

Overall, we performed numerical simulations for three series of experiments (44 models in total) by varying three controlling parameters (Table 2): 1) compositional (chemical) density contrast between the surrounding mantle and the plume ($\Delta\rho_0$); 2) width of the weak zone in the lithosphere above the plume (W_{WZ}); 3) externally applied extension (U_{EXT}). The first series (models 1.1-1.7) consists of experiments characterized by entirely weak lithosphere (the width of the weak zone is equal to the total horizontal extent of the model: W_{WZ} = 800 km), a neutral tectonic regime (no external extension: U_{EXT} = 0 cm yr^{-1}), and a chemical density contrast ($\Delta\rho_0$) varying between 0 and 300 kg m^{-3} with a step of 50 kg m^{-3}. Subsequently (the second series), we test different widths of the zone of weakness (W_{WZ}) – 50, 100, and 200 km (models 2.1.1-2.1.7, 2.2.1-2.2.7, and 2.3.1-2.3.7, respectively) – while keeping the other parameters as in the first set of models. Finally (the third series), we examine the velocity boundary conditions by varying the extension rate (U_{EXT}) from 0.25 to 2.0 cm yr^{-1} for four subsets of models with $\Delta\rho_0$ of 100 kg m^{-3} and 150 kg m^{-3} for W_{WZ} of 100 km (models 3.1.1-3.1.4 and 3.2.1-3.2.4, respectively) and $\Delta\rho_0$ of 50 kg m^{-3} and 100 kg m^{-3} for W_{WZ} of 200 km (models 3.3.1-3.3.4 and 3.4.1-3.4.4, respectively).

4. Results

4.1. Modes of plume-lithosphere interaction: from "mushroom" to "finger"

Our results suggest three modes of interaction between rheologically stratified continental lithosphere and small-scale secondary mantle plumes (Figs. 4–6, Videos 1-3 in Supplementary Materials). The first mode corresponds to horizontal spreading and flattening of the "mushroom"-shaped plume at the base of the lithosphere (Fig. 4a-c; Video 1 in Supplementary Materials) as commonly accepted in most conceptual models (e.g., Stern et al., 2020). The second scenario (Fig. 4d-f; Video 2 in Supplementary Materials) shows penetration of the "arrow"-shaped plume head through the overlying lithosphere, preceded by a relatively short-term (a few Myr) accumulation of plume material at the LAB. In the third case (Fig. 4g-i; Video 3 in Supplementary Materials), a columnar (or "finger"-shaped) ascent of the plume through the lithosphere begins immediately after reaching the lithospheric bottom and without ponding at the LAB as in the "mushroom" and, to some extent, the "arrow" scenarios. It is important to note that the final stages of development of both the "arrow"- and "finger"-shaped plumes are characterized by horizontal flow of the plume head, forming a shape similar to the "mushroom" but at much shallower depths near the Moho (Fig. 4f and Fig. 4i). In these cases, the resulting stress field subsequently leads to delamination and subsidence of the lithospheric mantle (see Videos 2-3 in the Supplementary Materials), which is a possible precursor to subduction initiation (Ueda et al., 2008; Cloetingh et al., 2021).

Below we present the results of a systematic parametric analysis of the factors controlling the transition between the different modes of plume-lithosphere interaction described above.

4.2. The first model series: varying density contrast, entirely weak lithosphere, no extension

Under the condition of a completely weak lithosphere (W_{WZ} = 800 km; see Fig. 5a-c and Fig. 6a, top row), the chemical density contrast between mantle and plume ($\Delta\rho_0$) is a key factor in determining the mode of plume-lithosphere interaction. When the compositional density deficit is absent or small, the purely thermal ($\Delta\rho_0$ = 0 kg m^{-3}) or only slightly hydrous ($\Delta\rho_0$ = 50 kg m^{-3}) plume has limited buoyancy, resulting in slow upwelling through the sublithospheric upper mantle (the rate is on the order of 3–4 cm yr^{-1}). Therefore, when the plume reaches the LAB, the thermal perturbation is small (<150 °C) and dissipates quickly. As a result, very limited thermal erosion affects only the lowermost ~10–20 km of the lithospheric mantle. In this "mushroom" case, the plume does not penetrate the lithosphere and spreads laterally below the LAB (Fig. 5a). For $\Delta\rho_0$ = 100 kg m^{-3}, the higher buoyancy leads to plume ascent rates of ~20 cm yr^{-1} and to an increase in plume dynamic pressure and thermal perturbation at the base of the lithosphere of up to 250 °C. Consequently, an initial short phase

Table 2
Controlling parameters and results of numerical experiments.

Model number	Controlling parameters			Model results
	Compositional deficit of the plume density, $\Delta\rho_0$ [kg m^{-3}]	Width of the weak zone in the lithosphere, W_{WZ} [km]	Rate of tectonic extension, U_{EXT} [cm yr^{-1}]	Mode of plume-lithosphere interaction: M – Mushroom A – Arrow F – Finger
1.1	0	800	0	M
1.2	50	800	0	M
1.3	100	800	0	A
1.4	150	800	0	F
1.5	200	800	0	F
1.6	250	800	0	F
1.7	300	800	0	F
2.1.1	0	50	0	M
2.1.2	50	50	0	M
2.1.3	100	50	0	M
2.1.4	150	50	0	M
2.1.5	200	50	0	M
2.1.6	250	50	0	M
2.1.7	300	50	0	M
2.2.1	0	100	0	M
2.2.2	50	100	0	M
2.2.3	100	100	0	M
2.2.4	150	100	0	A
2.2.5	200	100	0	F
2.2.6	250	100	0	F
2.2.7	300	100	0	F
2.3.1	0	200	0	M
2.3.2	50	200	0	M
2.3.3	100	200	0	A
2.3.4	150	200	0	F
2.3.5	200	200	0	F
2.3.6	250	200	0	F
2.3.7	300	200	0	F
3.1.1	100	100	0.25	M
3.1.2	100	100	0.5	A
3.1.3	100	100	1.0	A
3.1.4	100	100	2.0	F
3.2.1	150	100	0.25	A
3.2.2	150	100	0.5	A
3.2.3	150	100	1.0	F
3.2.4	150	100	2.0	F
3.3.1	50	200	0.25	M
3.3.2	50	200	0.5	A
3.3.3	50	200	1.0	A
3.3.4	50	200	2.0	A
3.4.1	100	200	0.25	A
3.4.2	100	200	0.5	A
3.4.3	100	200	1.0	F
3.4.4	100	200	2.0	F

of plume impingement at the LAB is followed by vertical upward penetration of the lithosphere with an “arrow”-like shape of the plume head (Fig. 5b). For larger density contrasts ($\Delta\rho_0$ > 150 kg m^{-3}), the rate of plume uplift reaches ~40 cm yr^{-1} with a resulting temperature difference at the LAB level exceeding 300 °C. The combined effect of increased chemical and thermal buoyancy precludes an impingement phase in which the plume stagnates at the base of the lithosphere. Instead, the hot and buoyant body of the plume enters directly into the lithospheric mantle, forming a peculiar “finger”-like shape of the thermal and density anomaly that may also be reflected in seismic tomographic images (Ritter et al., 2001). During the penetration phase, deformation is confined to a narrow sector around the plume, while the surrounding segments of the lithosphere remain largely unaffected. As mentioned above, in the last stage of the “finger” scenario, the plume undergoes lateral spreading with the “finger” gradually transforming into a “mushroom” at a shallow level near the base of the crust (Fig. 5c), in contrast to the classic “mushroom”-shaped plumes that stagnate at the LAB (Fig. 5a). This process of intra-lithospheric spreading of the plume material (Fig. 5c) is accompanied by a pronounced lateral propagation of the deformation of the lithospheric mantle, which may eventually lead to its delamination and foundering (see Video 3 in the Supplementary Materials).

4.3. The second model series: varying density contrast and width of weak block, no extension

In addition to plume density contrasts, laterally varying rheological properties in the overlying plate may also be an important parameter that can significantly affect the ability of the plume to penetrate the lithosphere as well as the style of that penetration

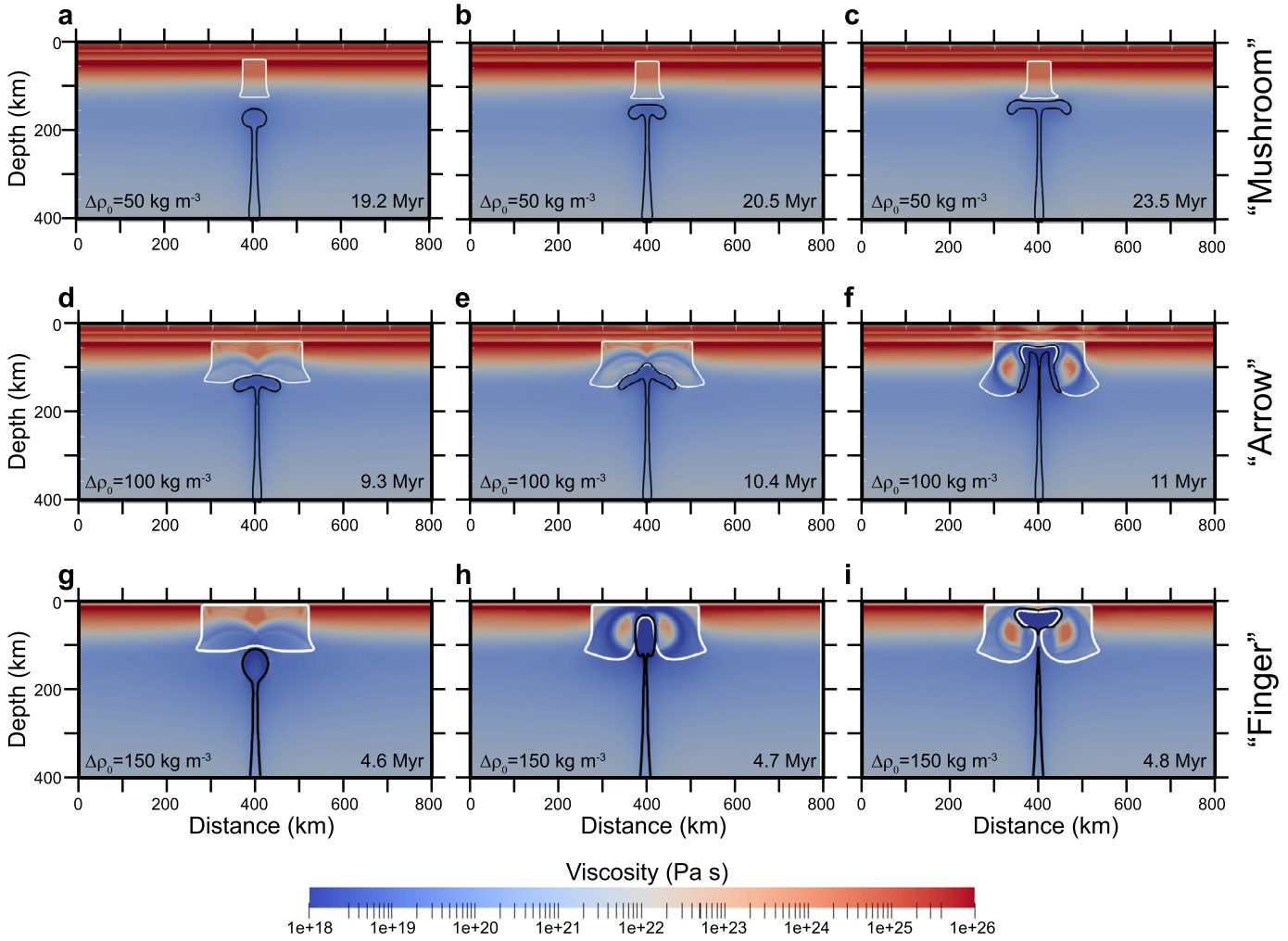

Fig. 4. Temporal evolution of representative models (shown as viscosity distributions) for three modes of interaction between relatively small secondary plume and the overlying continental lithosphere: a-c) "mushroom" mode: $\Delta\rho_0$ = 50 kg m^{-3}, W_{WZ} = 50 km; d-f) "arrow" mode: $\Delta\rho_0$ = 100 kg m^{-3}, W_{WZ} = 200 km; and g-i) "finger" mode: $\Delta\rho_0$ = 150 kg m^{-3}, W_{WZ} = 200 km. The black line represents the boundary of the upwelling plume material, while the white line represents the edges of the weak zone in the lithosphere.

(e.g., Beniest et al., 2017). In this set of experiments, we simulated the presence of a weak sector in the lithospheric mantle, that has a limited horizontal extent (in contrast to the unbounded extent in the previous series of models with a completely weak overlying plate) and is located directly above the plume. The width of this weak zone (W_{WZ}) varies from 50 km (not shown) through 100 km (Fig. 5g-i) to 200 km (Fig. 5d-f). As mentioned above, the occurrence of such a weak block could reflect drastic local softening of the lithosphere by the melting generated in the rising mantle plume (Gerya et al., 2015). Alternatively, it may simply be a structural discontinuity inherited from previous tectonic events.

When W_{WZ} is 50 km, the mantle plume always stagnates at the base of the lithosphere (Fig. 6a, bottom row). Even when $\Delta\rho_0$ is set to the maximum value (300 kg m^{-3}), the effect of plume erosion at the base of the weak lithospheric zone is limited to a thickness of ~20 km, which becomes even smaller for lower values of $\Delta\rho_0$. In contrast, for a larger extent of the weak zone (W_{WZ} = 100–200 km), plume buoyancy may exceed the strength of the lithosphere. In these cases, the resulting mode of the interaction between the plume and the lithosphere depends on how the density deficit of the plume ($\Delta\rho_0$) and the geometric characteristics of the pre-imposed lithospheric weakness (W_{WZ}) are combined in each individual experiment (Fig. 6a, middle rows). For W_{WZ} of 200 km, a $\Delta\rho_0$ of 100 kg m^{-3} is sufficient to cause plume penetration into the lithosphere (Fig. 5e), whereas a narrower (W_{WZ} = 100 km) zone of weakness requires a higher (150 kg m^{-3}) value of $\Delta\rho_0$ (Fig. 5h). These combinations of $\Delta\rho_0$ and W_{WZ} mark the transition between the mode of "mushroom"-shaped plume (permanent stagnation at the LAB) and the "arrow"-like shape of the plume (short phase of lateral spreading at the base of the lithosphere, followed by vertical penetration toward shallower lithospheric levels). As $\Delta\rho_0$ and/or W_{WZ} incrementally increased (Fig. 5f and Fig. 5i), there is no phase of plume flattening at the LAB, indicating a "finger" mode. For $\Delta\rho_0 \geq$ 200 kg m^{-3}, the mode of the "finger"-shaped plume remains stable for both W_{WZ} = 100 km and W_{WZ} = 200 km (Fig. 6a, middle rows). It is noteworthy that the lateral intra-lithospheric spreading of the plume material in the last stage of the "arrow" and "finger" modes is limited to the horizontal extent of the weak zone (see Video 2 in the Supplementary Materials).

4.4. The third model series: varying tectonic extension for different density contrasts and widths of weak zone

The lithospheric stress field is included in our analysis by applying the extension at the plate boundaries in some simulation settings (Fig. 6b) to evaluate its effects on the characteristic features of the explored system. We tested different values of tectonic

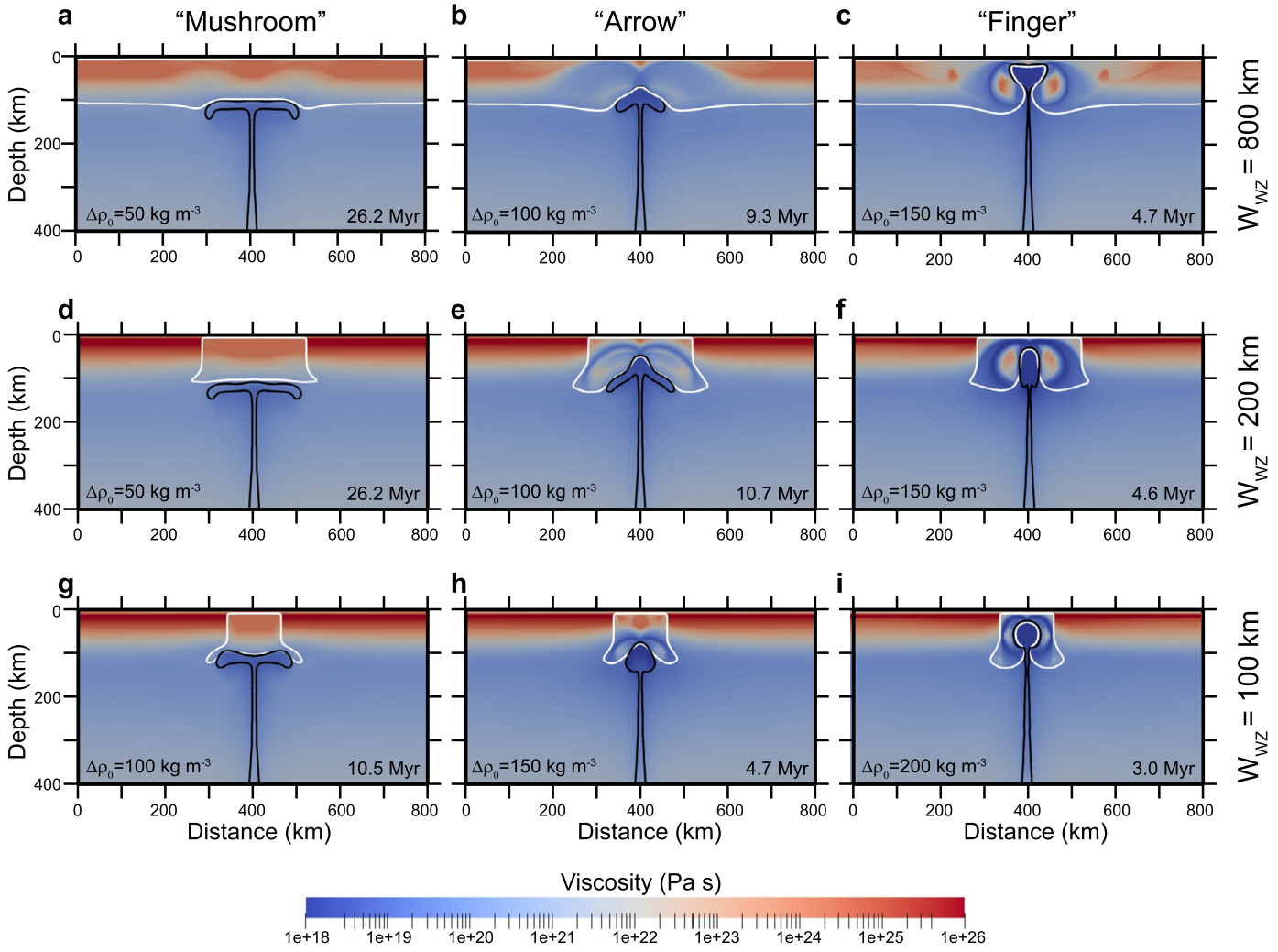

Fig. 5. Modelled viscosity distributions for the experiments with different combinations of chemical density contrasts ($\Delta\rho_0$) and widths of the weak zone (W_{WZ}). An increase in density contrast ($\Delta\rho_0$) favours the transition from "mushroom" (left column) to "arrow" (middle column) and then to "finger" (right column) mode of system development. Note that for broader zones of weakness (higher W_{WZ}), a smaller compositional density deficit (lower $\Delta\rho_0$) is sufficient to cause penetration of the plume into the lithosphere.

extension rate (U_{EXT}) ranging from 0.25 to 2.0 cm yr^{-1} in combination with $\Delta\rho_0$ between 50 kg m^{-3} and 150 kg m^{-3}, and W_{WZ} of 100 km and 200 km. These ranges of values for a $\Delta\rho_0$ and W_{WZ} were chosen because, if no extension is implemented, they correspond to the most important transition in model behaviour (Fig. 6a) from plume underplating when a plume cannot pass through the lithosphere ("mushroom" scenario) to the situation in which the positively buoyant plume starts to overcome the strength of the overlying plate and penetrates it ("arrow" scenario).

The general tendency, which holds for all combinations of $\Delta\rho_0$ and W_{WZ}, is that tectonic extensional stresses facilitate plume penetration into the lithosphere, as evidenced by the systematic shift in interaction mode from "mushroom" to "arrow" and from "arrow" to "finger" with increasing U_{EXT} (Fig. 6b). Importantly, a low U_{EXT} value (0.25 cm yr^{-1}) does not change the mode compared to the tectonically neutral regime. A further increase in U_{EXT} to 0.5 cm yr^{-1} results in a conversion of the original "mushroom" mode of the settings with low $\Delta\rho_0$ (50 kg m^{-3}) or W_{WZ} (100 km) to the "arrow" mode. For U_{EXT} of 1.0 cm yr^{-1}, the mode of the system becomes "finger" at higher $\Delta\rho_0$ (150 kg m^{-3}) or W_{WZ} (200 km). The maximum value of U_{EXT} (2.0 cm yr^{-1}) leads to the "finger" mode for all tested combinations of $\Delta\rho_0$ or W_{WZ}, except for the lowest $\Delta\rho_0$ (50 kg m^{-3}), where it remains the "arrow", as for U_{EXT} of 0.5–1.0 cm yr^{-1} (Fig. 6b).

5. Discussion

5.1. Comparison between modelling results and seismo-tomographic observations

Apart from the classic scenario in which the plume head spreads horizontally to form a "mushroom"-shaped plume at the lithospheric bottom, our experiments reveal that, given a suitable combination of initial and boundary conditions, the plume material can also penetrate the lithosphere vertically up to shallow depths near the Moho developing "arrow" and "finger"-shaped structures within the lithosphere. These results have led us to compare three characteristic secondary mantle plumes observed in the upper mantle underlying different regions of the Eurasian plate (Fig. 7; right panels) with modelled modes of atypical ("arrow" and "finger") plume emplacement (Fig. 7; left panels).

The first prominent example is the Tengchong volcano (Fig. 7a), where a low velocity seismic anomaly rises from the MTZ to the

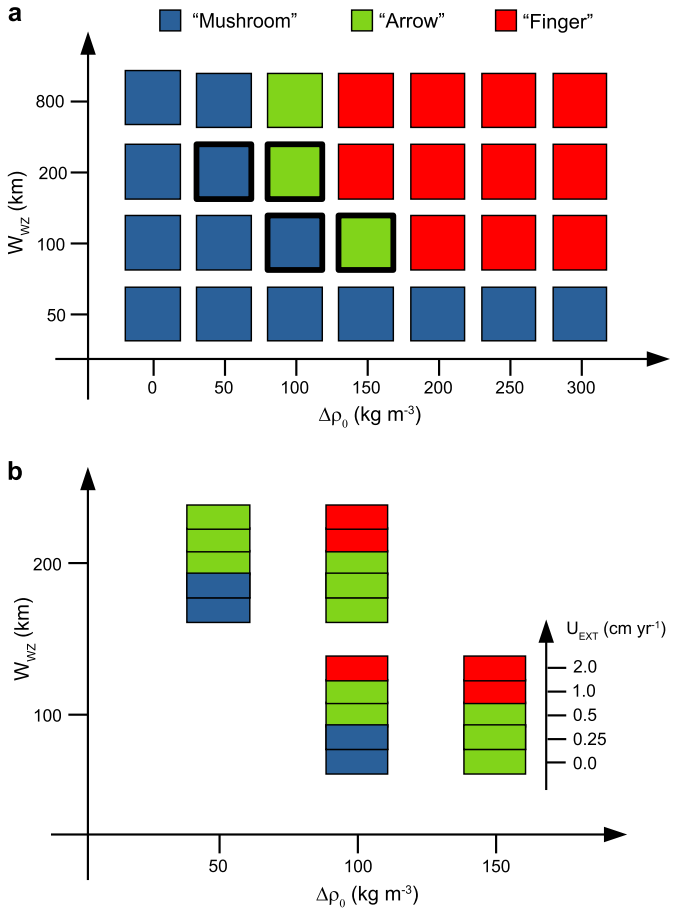

Fig. 6. Modes of plume-lithosphere interaction as a function of initial compositional density contrast ($\Delta\rho_0$), weak zone width (W_{WZ}), and tectonic extension (U_{EXT}). a) The parameter space of $\Delta\rho_0$ ranges from 0 to 300 kg m^{-3} and of W_{WZ} from 50 to 800 km, systematically covered for the tectonically neutral regime (U_{EXT} = 0 cm yr^{-1}). b) U_{EXT} from 0.25 to 2.0 cm yr^{-1} tested for the cases with combinations of $\Delta\rho_0$ and W_{WZ} corresponding to the transition between "mushroom" and "arrow" scenarios for U_{EXT} = 0 cm yr^{-1} (bold rectangles in panel "a").

surface, traversing the overlying sublithospheric and lithospheric mantle. Importantly, vertical uplift there is accompanied by horizontal deflection of plume material from the main column toward the SW, with accumulation at the LAB level, creating an asymmetric, one-sided "arrow"-shaped plume head (Fig. 7a, right panel) that resembles the corresponding mode of plume-lithosphere interaction detected in our study (Fig. 7a, left panel). We note, however, that the structure of the Tengchong plume may look different in differently oriented cross-sections (e.g., in the N-S section it forms a simple "finger" without an "arrow"-shaped component; Fig. 2e, middle panel). Therefore, more detailed 3D modelling will be required in the future to adequately capture and reproduce the complex and ambiguous configuration of the Tengchong plume.

The second example is from the ECRIS where the "finger" mode finds its archetypal equivalent in the plume below the Eifel volcanic field (Fig. 7b). Here the upper mantle is characterized by vertical penetration of plume material in the form of a narrow column extending from the MTZ to the shallowest lithospheric levels, with no evidence of ponding or accumulation near the LAB.

The final (third) example is the somewhat enigmatic intra-lithospheric "mushroom" beneath the Changbaishan volcanic area (Fig. 7c, right panel), which should not be confused with the classic "mushroom"-shaped flattening of plumes below the LAB (e.g., Stern et al., 2020). We interpret this Changbaishan anomaly as a later stage development of the "finger"-shaped plume, characterized by lateral spreading of its head at relatively shallow depths inside the lithosphere (Fig. 7c, left panel). Importantly, similar intra-lithospheric anomalies, indicating horizontal flow of plume material at shallower levels than the LAB, are also reported for the Hainan (see Fig. 2c, profiles NW-SE and S-N) and Tengchong (see interpretive cross-section in Fig. 2e, bottom panel) plumes. This feature therefore could be quite common and warrants a more detailed future investigation through both observations and modelling.

5.2. Hydrous component as key to the "finger"-shaped intra-lithospheric anomalies

Our modelling shows that the buoyancy forces of purely thermal or only slightly hydrous plumes are insufficient to overcome the strength of the continental lithosphere. Under a tectonically neutral regime, therefore, they all develop in a "mushroom" mode, even when the overlying plate is completely weak (Fig. 6a, two left columns). These results are in apparent contradiction to previous analyses of purely thermal anomalies (Burov and Cloetingh, 2009), that show that they are capable of vertical ascent through the continental lithosphere. However, it is important to note that the plumes in Burov and Cloetingh (2009) were much larger (initial radius of 100 km) than the typical secondary plumes investigated in our work and, more importantly, were assumed to have extremely high temperatures (up to 2200 °C). Such high temperatures, however, are well above petrologic constraints on the maximum excess temperature of plumes in the Earth's upper mantle (400 °C; Thompson and Gibson, 2000). More recent studies of small-scale anomalies with realistic temperature contrasts of 200–300 °C (Herzberg and Gazel, 2009) have shown that purely thermal secondary plumes can actively penetrate the lithosphere only under conditions of applied far-field extension with a half-rate of $\geq$ 0.3 cm yr^{-1}, while stagnating at the base of unstressed lithosphere (Koptev et al., 2021a). These findings are consistent with the results of our experiments.

In this context, the chemical (hydrous) component of plume buoyancy is shown to be the most important factor in the transition from the "mushroom" mode of system evolution to cases where plume material penetrates vertically into the lithospheric mantle up to depths near the Moho ("arrow" and "finger" modes; see Fig. 5). Another crucial ingredient is the presence and width of a zone of weakness in the lithospheric segment above the thermochemical plume. To establish the "arrow" mode, a compositional density deficit of 100 kg m^{-3} is sufficient when the weak zone is as wide as 200 km, whereas it must be increased to 150 kg m^{-3} when the zone of weakness is reduced to 100 km. Further increasing the chemical density contrast and the width of the weak zone favours the development of a "finger"-shaped plume (Fig. 6a). Importantly, a narrow zone of lithospheric weakness (50 km) appears to be insufficient to allow any kind of plume penetration into the lithosphere (neither "arrow" nor "finger") for all density contrasts tested in our study, including the maximum of 300 kg m^{-3} (Fig. 6a, bottom row). Given that the width of the weak zone required for plume penetration should be at least two times (100 km) greater than the lateral extent of the plume head at the time of reaching the LAB (50 km), it is unlikely that magmatic weakening caused by partial melting in the plume (Gerya et al., 2015) can generate the necessary weakness in the lithosphere alone. Therefore, the presence of pre-existing structures formed during previous tectonic events should also be considered as a factor in local weakening of the lithosphere.

In agreement with findings from a previous study (Koptev et al., 2021a), far-field forces acting at the boundaries of the lithosphere facilitate penetration of the plume up to the surface. In particular, the increase in tectonic extension from a half-rate of 0.5 to 2.0 cm yr^{-1} systematically shifts the plume-lithosphere in-

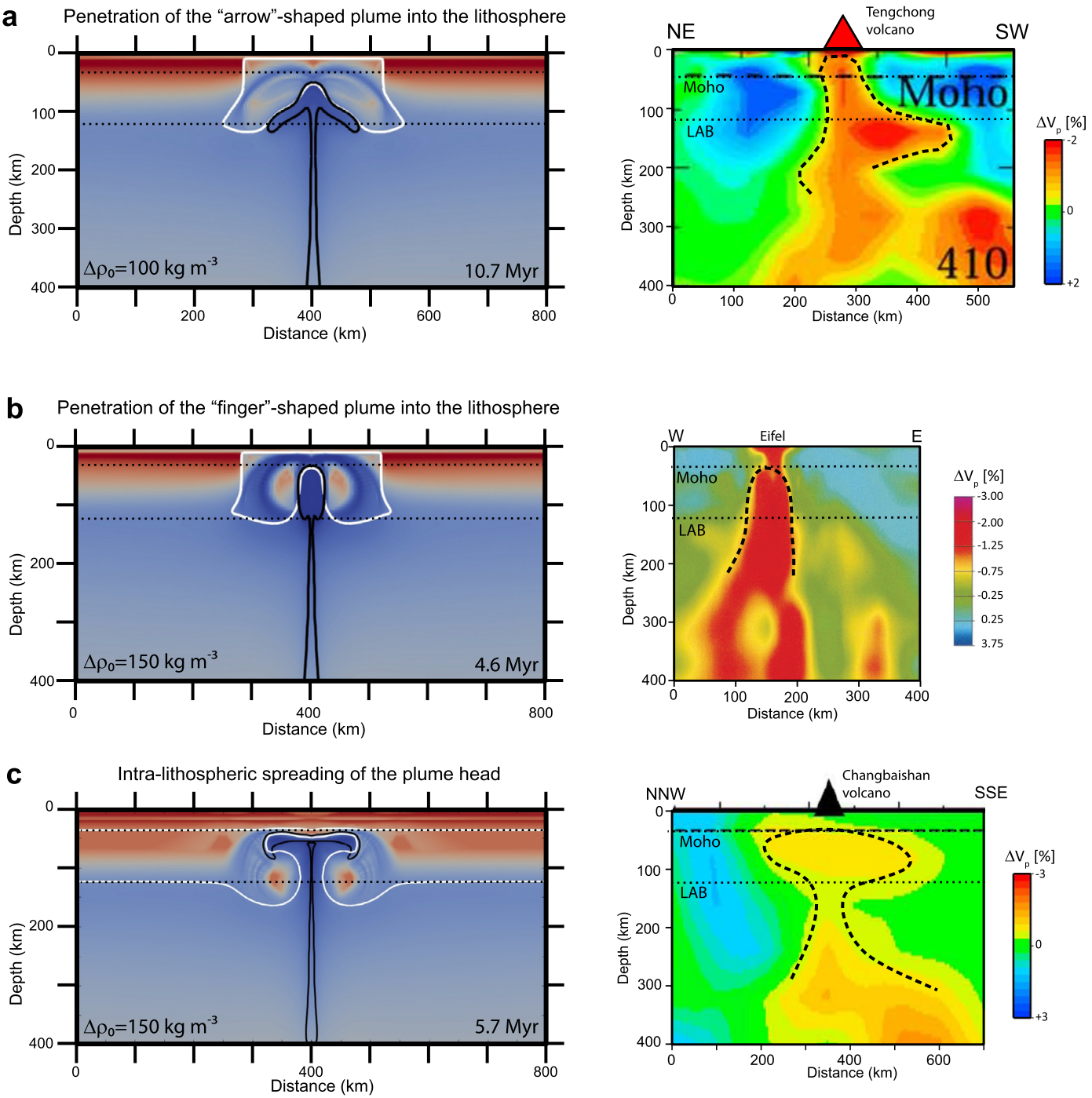

Fig. 7. Comparison of modelled plume-emplacement modes (left panels) with natural examples of seismic velocity anomalies in the upper mantle (right panels). a) Modelled "arrow"-shaped plume vs. asymmetric "arrow" beneath the Tengchong volcano. b) Modelled "finger"-shaped plume vs. columnar structure in sublithospheric and lithospheric mantle below the Eifel volcanic fields. c) Advanced stage of the "finger" scenario with intra-lithospheric spreading of the plume head vs. intra-lithospheric "mushroom" underlying the Changbaishan volcanic area.

teraction mode from "mushroom" to "arrow" and from "arrow" to "finger" (Fig. 6b). However, our modelling results also demonstrate the possibility of "arrow" and even "finger" modes without strong (a half-rate of $\geq$ 0.5 cm yr^{-1}) extension. Under the condition of appropriate combinations of density contrast and weak zone width, the vertical rise of the plume through the lithosphere occurs even in a tectonically neutral regime or with a very slow extension (a half-rate of 0.25 cm yr^{-1}) (Fig. 6). Such low rates of tectonic extension are typical of present-day continental rifts (Saria et al., 2014), developing without exposure to high levels of far-field stresses and mainly due to gradients of gravitational potential energy within the lithosphere (Koptev and Ershov, 2010). The observations of "finger"-shaped plumes in the interior of the lithosphere underneath the ECRIS (Granet et al., 1995; Ritter et al., 2001) can be seen as a natural confirmation that strong far-field induced extension is not mandatory for the formation of such structures.

In contrast to tectonic extension, the compositional deficit of the plume density appears to be a characteristic feature to reproduce the "finger"-like behaviour in the model. This is in line with

aqueous geochemical signatures indicating fluid-enriched components in volcanism associated with secondary plumes. Importantly, these hydrous plumes are not restricted to areas overlying present-day or recently subducted slabs (Kuritani et al., 2011, 2019), such as the East Asian region surrounded by double-sided subduction zones consisting of the Western Pacific and Sumatra trench systems (Safonova et al., 2015). A hydrous mantle source is also demonstrated for the magmatic centres in Europe (Gu et al., 2018; Kovács et al., 2020). The low observed heat flow in the Eifel volcanic field and mantle outgassing in the Bohemian Massif are additional arguments for a hydrous nature of the ECRIS plumes formed in a continental foreland on the subducting plate (Ziegler and Dèzes, 2007).

6. Conclusions and further research directions

Based on a series of numerical experiments combined with an overview of available seismological, geological, and geochemical data, we conclude that small-scale secondary plumes are typically hydrous in nature and that their occurrence is not restricted to a particular tectonic or regional setting. Apart from the evidence reported for regions such as Europe and East Asia, further investigation on a global scale is warranted. We predict that a variety of new secondary plumes will be found in nature, with various modes of emplacement beneath or into the overlying lithosphere. In this regard, future high-resolution seismic tomographic studies in continental and oceanic lithospheric environments and their integration with petrologic and geochemical constraints will be of particular importance for discovering new secondary plumes and elucidating their formation mechanisms.

CRediT authorship contribution statement

All persons who meet authorship criteria are listed as authors, and all authors certify that they have participated sufficiently in the work to take public responsibility for the content, including participation in the concept, design, analysis, writing, or revision of the manuscript. Furthermore, each author certifies that this material or similar material has not been and will not be submitted to or published in any other publication before its appearance in the Earth and Planetary Science Letters.

Declaration of competing interest

The authors declare that they have no known competing financial interests or personal relationships that could have appeared to influence the work reported in this paper.

Data availability

Data will be made available on request.

Acknowledgements

This study is co-funded by an Alexander von Humboldt Foundation fellowship to A. Koptev and by Project PRIN n. 201743P29 FLUIDS (Detection and tracking of crustal fluid by multi-parametric methodologies and technologies) to A. Lavecchia. S. Cloetingh was supported by the Distinguished Guest Scientist Fellowship Program of the Hungarian Academy of Sciences and an Alexander von Humboldt Foundation research award. The authors acknowledge the support of the MTA FI Lendület Pannon LitH$_2$Oscope and NKFIH NN 141956 TopoTransylvania grants. We are grateful to the editor Prof. J.-P. Avouac and an anonymous reviewer for insightful and constructive suggestions.

Appendix A. Methods

We performed the numerical simulations presented in this paper using the thermo-mechanical code ASPECT 2.3.0 (Kronbichler et al., 2012). In the following, we give the governing equations solved by this code and describe the assumed rheology.

a) Governing equations

Our model is governed by the equations of momentum, mass and energy in a compressible medium, solved over the domain Ω:

$$-\nabla \cdot \left[2\eta\left(\dot{\varepsilon}\left(\boldsymbol{u}\right) - \frac{1}{3}\left(\nabla \cdot \boldsymbol{u}\right)\mathbf{1}\right)\right] + \nabla p = \rho \boldsymbol{g} \tag{1}$$

$$\nabla \cdot \left(\rho \boldsymbol{u}\right) = 0 \tag{2}$$

$$\rho C_p \left(\frac{\partial T}{\partial t} + \boldsymbol{u} \cdot \nabla T\right) - \nabla \cdot k \nabla T = \alpha T \left(\boldsymbol{u} \cdot \nabla p\right), \tag{3}$$

where η is viscosity, $\dot{\varepsilon}\left(\boldsymbol{u}\right) = \frac{1}{2}(\nabla \boldsymbol{u} + \nabla \boldsymbol{u}^T)$ is the symmetric gradient of the velocity (i.e. strain rate), $\boldsymbol{u}$ is velocity, p is pressure, ρ is density, $\boldsymbol{g}$ is the acceleration due to gravity (9.81 m s^{-2}), C_p is heat capacity, T is temperature, k is thermal conductivity, α is thermal expansion.

Density is temperature-dependent, according to the formula:

$$\rho\left(T\right) = \rho_0\left[1 - \alpha\left(T - T_0\right)\right], \tag{4}$$

where ρ_0 is the value of the rock density at a reference temperature T_0. Thermal parameters and reference density values are given in Tables A.1 and A.2.

The upper and lower crust, the lithospheric and sublithospheric mantle, the weak zone, and the plume represent the elements (c_i) of the composition field, which are passively advected according to the equation:

$$\frac{\partial c_i}{\partial t} + \boldsymbol{u} \cdot \nabla c_i = 0 \tag{5}$$

The code adopts the finite element method for these equations. The temperature and composition equations are solved once at the beginning of each time step. Afterwards, an iterative solver is implemented for the momentum and mass equations (e.g., Bangerth et al., 2021).

b) Rheology

The model implements a nonlinear, composite visco-plastic rheology for Earth materials, where the viscous rheological component is defined by the following equation (e.g., Billen and Hirth, 2007):

$$\eta = \frac{1}{2} A^{-\frac{1}{n}} d^{\frac{m}{n}} \dot{\varepsilon}_{II}^{\frac{1-n}{n}} exp\left(\frac{E + pV}{nRT}\right) \tag{6}$$

where A is Dorn parameter, n is power law creep exponent, d is grain size, m is grain size exponent, $\dot{\varepsilon}_{II} = \sqrt{\frac{1}{2}\dot{\varepsilon}'_{ij}\dot{\varepsilon}'_{ij}}$ is effective deviatoric strain rate, E is activation energy, V is activation volume, and R is the gas constant (8.314 J K^{-1} mol^{-1}). In our study, we consider deformation by both diffusion (n = 1, m > 1) and dislocation (n > 1, m = 0) creep. The values of the adopted parameters can be found in Table A.3.

We limit the values of viscous stress by adopting a plasticity mechanism through a Drucker-Prager criterion, where the yield stress (σ_y) in 2D is equivalent to the Mohr-Coulomb yield surface:

$$\sigma_y = C cos\left(\varphi\right) + P sin(\varphi) \tag{7}$$

Table A.1
Thermal parameters.

Compositional unit	Heat capacity, Cp [J K^{-1} kg^{-1}]	Thermal conductivity, k [W m^{-1} K^{-1}]	Thermal expansion, α [K^{-1}]
Upper crust	750 *	2.7 •	$2.5{\cdot}10^{-5}$ *
Lower crust	750 *	2.7 •	$2.5{\cdot}10^{-5}$ *
Lithospheric mantle	1250 *	3.0 •	$3.0{\cdot}10^{-5}$ *
Sublithospheric mantle	1250 *	3.3 •	$3.0{\cdot}10^{-5}$ *
Mantle plume	1250 *	3.3 •	$3.0{\cdot}10^{-5}$ *
Weak zone	1250 *	3.0 •	$3.0{\cdot}10^{-5}$ *

* Bangerth et al., 2021; • Clauser and Huenges, 1995.

Table A.2
Reference density and brittle rheological parameters.

Compositional unit	Reference density, ρ_0 [kg m^{-3}]	Cohesion, C [MPa]	Internal friction angle, φ [°]
Upper crust	2800 ‡	20 *	20 *
Lower crust	2900 ‡	20 *	20 *
Lithospheric mantle	3300 $	20 *	20 *
Sublithospheric mantle	3300 $	20 *	20 *
Mantle plume	3000 – 3300 @	20 *	20 *
Weak zone	3300 $	2 &	3 &

‡ Carmichael, 2017; $ Gerya, 2019; @ Baes et al., 2016; * Bangerth et al., 2021; & Koptev et al., 2019.

Table A.3
Ductile rheological parameters.

Compositional unit	Dorn parameter, A [MPa^{-n} s^{-1}]	Power law creep exponent, n []	Activation energy, E [kJ mol^{-1}]	Activation volume, V [cm^3 mol^{-1}]
Upper crust	$1.0\ 10^{-3}$ †	2 †	167 †	0 †
Lower crust	$3.27{\cdot}10^{-4}$ †	3.2 †	238 †	0 †
Lithospheric mantle	$1.1{\cdot}10^{5}$ (disl.)	3.5 (disl.)	530 (disl.)	17 (disl.)
	$2.46\ 10^{-10}$ (diff.)	1 (diff.)	375 (diff.)	10 (diff.)
Sublithospheric mantle	$1.1{\cdot}10^{5}$ (disl.)	3.5 (disl.)	530 (disl.)	20 (disl.)
	$2.46\ 10^{-10}$ (diff.)	1 (diff.)	375 (diff.)	10 (diff.)
Mantle plume	$1.1{\cdot}10^{5}$ (disl.)	3.5 (disl.)	530 (disl.)	20 (disl.)
	$2.46\ 10^{-10}$ (diff.)	1 (diff.)	375 (diff.)	10 (diff.)
Weak zone	$1.1{\cdot}10^{5}$ (disl.)	3.5 (disl.)	530 (disl.)	20 (disl.)
	$2.46\ 10^{-10}$ (diff.)	1 (diff.)	375 (diff.)	10 (diff.)

The ductile rheology of the mantle lithosphere (including the weak zone) is controlled mainly by dislocation creep ("disl."), whereas the sublithospheric mantle (including the mantle plume) deforms predominantly by diffusion creep ("diff.") with a grain size (d) of 1.0 mm and a grain size exponent (m) of 3.
Values are taken from Hirth and Kohlstedt (1995, 2004), except for those marked (†), which are from Shelton et al. (1981).

where C is cohesion, P is pressure, and φ is internal friction angle (see Table A.2).

The resulting viscosity is assigned by means of a Christmas tree-like criterion, where the rheological behaviour depends on the minimum between the ductile and brittle/plastic components (Ranalli, 1995; Burov, 2011): when the viscous stress ($\sigma = 2\eta\dot{\varepsilon}_{II}$) exceeds the yield stress (σ_y), the viscosity is recalculated as follows (e.g., Thieulot, 2011):

$$\eta = \eta_y = \frac{\sigma_y}{2\dot{\varepsilon}_{II}} \tag{8}$$

Appendix B. Supplementary material

Supplementary material related to this article can be found online at https://doi.org/10.1016/j.epsl.2022.117819.

References

Baes, M., Gerya, T., Sobolev, S.V., 2016. 3-D thermo-mechanical modeling of plume-induced subduction initiation. Earth Planet. Sci. Lett. 453, 193–203.

Baes, M., Sobolev, S., Gerya, T., Brune, S., 2020. Plume-induced subduction initiation: single-slab or multi-slab subduction? Geochem. Geophys. Geosyst. 21 (2), e2019GC008663.

Beniest, A., Koptev, A., Leroy, S., Sassi, W., Guichet, X., 2017. Two-branch break-up systems by a single mantle plume: insights from numerical modeling. Geophys. Res. Lett. 44 (19), 9589–9597.

Blum, J., Shen, Y., 2004. Thermal, hydrous, and mechanical states of the mantle transition zone beneath southern Africa. Earth Planet. Sci. Lett. 217 (3–4), 367–378.

Burov, E., Cloetingh, S., 2009. Controls of mantle plumes and lithospheric folding on modes of intraplate continental tectonics: differences and similarities. Geophys. J. Int. 178 (3), 1691–1722.

Cloetingh, S., Koptev, A., Kovács, I., Gerya, T., Beniest, A., Willingshofer, E., Ehlers, T.A., Andrić-Tomašević, N., Botsyun, S., Eizenhöfer, P.R., François, T., Beekman, F., 2021. Plume-induced sinking of intracontinental lithospheric mantle: an overlooked mechanism of subduction initiation? Geochem. Geophys. Geosyst. 22 (2), e2020GC009482.

Courtillot, V., Davaille, A., Besse, J., Stock, J., 2003. Three distinct types of hotspots in the Earth's mantle. Earth Planet. Sci. Lett. 205 (3–4), 295–308.

Dannberg, J., Sobolev, S.V., 2015. Low-buoyancy thermochemical plumes resolve controversy of classical mantle plume concept. Nat. Commun. 6 (1), 6960.

Dingwell, D., 1995. Viscosity and anelasticity of melts. In: Ahrens, T.J. (Ed.), Mineral Physics and Crystallography. A Handbook of Physical Constants. AGU Reference Shelf 2. Am. Geophys. Union, Washington, DC, pp. 209–217.

Drewitt, J.W., Walter, M.J., Brodholt, J.P., Muir, J.M., Lord, O.T., 2022. Hydrous silicate melts and the deep mantle H2O cycle. Earth Planet. Sci. Lett. 581, 117408.

Forte, A.M., Mitrovica, J.X., 1996. New inferences of mantle viscosity from joint inversion of long-wavelength mantle convection and post-glacial rebound data. Geophys. Res. Lett. 23 (10), 1147–1150.

Freitas, D., Manthilake, G., Schiavi, F., Chantel, J., Bolfan-Casanova, N., Bouhifd, M.A., Andrault, D., 2017. Experimental evidence supporting a global melt layer at the base of the Earth's upper mantle. Nat. Commun. 8 (1), 2186.

Fukao, Y., Obayashi, M., Nakakuki, T., Deep Slab Project Group, 2009. Stagnant slab: a review. Annu. Rev. Earth Planet. Sci. 37, 19–46.

Gaillard, F., Sator, N., Gardés, E., Guillot, B., Massuyeau, M., Sifré, D., Hammouda, T., Richard, G., 2019. The link between the physical and chemical properties of carbon-bearing melts and their application for geophysical imaging of

Earth's mantle. In: Deep Carbon: Past to Present. Cambridge University Press, pp. 163–187.
Gerya, T.V., Connolly, J.A., Yuen, D.A., Gorczyk, W., Capel, A.M., 2006. Seismic implications of mantle wedge plumes. Phys. Earth Planet. Inter. 156 (1–2), 59–74.
Gerya, T.V., Stern, R.J., Baes, M., Sobolev, S.V., Whattam, S.A., 2015. Plate tectonics on the Earth triggered by plume-induced subduction initiation. Nature 527 (7577), 221–225.
Ghosh, D., Maiti, G., Mandal, N., Baruah, A., 2020. Cold plumes initiated by Rayleigh-Taylor instabilities in subduction zones, and their characteristic volcanic distributions: the role of slab dip. J. Geophys. Res., Solid Earth 125 (8), e2020JB019814.
Glerum, A., Brune, S., Stamps, D.S., Strecker, M.R., 2020. Victoria continental microplate dynamics controlled by the lithospheric strength distribution of the East African Rift. Nat. Commun. 11, 2881.
Granet, M., Wilson, M., Achauer, U., 1995. Imaging a mantle plume beneath the French Massif Central. Earth Planet. Sci. Lett. 136 (3–4), 281–296.
Gu, X., Ingrin, J., Deloule, E., France, L., Xia, Q., 2018. Metasomatism in the subcontinental lithospheric mantle beneath the south French Massif Central: constraints from trace elements, Li and H in peridotite minerals. Chem. Geol. 478, 2–17.
Hack, A.C., Thompson, A.B., 2011. Density and viscosity of hydrous magmas and related fluids and their role in subduction zone processes. J. Petrol. 52 (7–8), 1333–1362.
Hawkesworth, C.J., Turner, S.P., McDermott, F., Peate, D.W., Van Calsteren, P., 1997. U-Th isotopes in arc magmas: implications for element transfer from the subducted crust. Science 276 (5312), 551–555.
Helffrich, G.R., Wood, B.J., 2001. The Earth's mantle. Nature 412 (6846), 501–507.
Herzberg, C., Gazel, E., 2009. Petrological evidence for secular cooling in mantle plumes. Nature 458 (7238), 619–622.
Karato, S.I., Jacobsen, S.D., Van Der Lee, S., 2006. Influence of hydrogen-related defects on the electrical conductivity and plastic deformation of mantle minerals: a critical review. In: American Geophysical Union. In: Geophysical Monograph Series, vol. 168, pp. 113–129.
Koppers, A.A., et al., 2021. Mantle plumes and their role in Earth processes. Nat. Rev. Earth Environ. 2 (6), 382–401.
Koptev, A., Calais, E., Burov, E., Leroy, S., Gerya, T., 2018. Along-axis variations of rift width in a coupled lithosphere-mantle system, application to East Africa. Geophys. Res. Lett. 45 (11), 5362–5370.
Koptev, A., Calais, E., Burov, E., Leroy, S., Gerya, T., 2015. Dual continental rift systems generated by plume-lithosphere interaction. Nat. Geosci. 8, 388–392.
Koptev, A., Cloetingh, S., Ehlers, T.A., 2021a. Longevity of small-scale ("baby") plumes and their role in lithospheric break-up. Geophys. J. Int. 227 (1), 439–471.
Koptev, A., Cloetingh, S., Kovács, I.J., Gerya, T., Ehlers, T.A., 2021b. Controls by rheological structure of the lithosphere on the temporal evolution of continental magmatism: inferences from the Pannonian Basin system. Earth Planet. Sci. Lett. 565, 116925.
Koptev, A.I., Ershov, A.V., 2010. The role of the gravitational potential of the lithosphere in the formation of a global stress field. Izv. Phys. Solid Earth 46 (12), 1080–1094.
Kovács, I., et al., 2020. The role of water and compression in the genesis of alkaline basalts: inferences from the Carpathian-Pannonian region. Lithos 354–355, 105323.
Kronbichler, M., Heister, T., Bangerth, W., 2012. High accuracy mantle convection simulation through modern numerical methods. Geophys. J. Int. 191 (1), 12–29.
Kumagai, I., Davaille, A., Kurita, K., Stutzmann, E., 2008. Mantle plumes: thin, fat, successful, or failing? Constraints to explain hot spot volcanism through time and space. Geophys. Res. Lett. 35 (16), L16301.
Kuritani, T., Ohtani, E., Kimura, J.I., 2011. Intensive hydration of the mantle transition zone beneath China caused by ancient slab stagnation. Nat. Geosci. 4 (10), 713–716.
Kuritani, T., et al., 2019. Buoyant hydrous mantle plume from the mantle transition zone. Sci. Rep. 9 (1), 1–7.
Lavecchia, A., Thieulot, C., Beekman, F., Cloetingh, S., Clark, S., 2017. Lithosphere erosion and continental breakup: interaction of extension, plume upwelling and melting. Earth Planet. Sci. Lett. 467, 89–98.
Lei, J., Zhao, D., Steinberger, B., Wu, B., Shen, F., Li, Z., 2009a. New seismic constraints on the upper mantle structure of the Hainan plume. Phys. Earth Planet. Inter. 173 (1–2), 33–50.
Lei, J., Zhao, D., Su, Y., 2009b. Insight into the origin of the Tengchong intraplate volcano and seismotectonics in southwest China from local and teleseismic data. J. Geophys. Res., Solid Earth 114 (B5), B05302.
Liu, J., Xia, Q.K., Sun, H., Hanski, E., Kuritani, T., Gu, X.Y., Chen, H., 2022. Compositional variation of picrites in the Emeishan large igneous province modulated by water in the mantle plume. J. Geophys. Res., Solid Earth 127 (1), e2021JB023584.
Maguire, R., Ritsema, J., van Keken, P.E., Fichtner, A., Goes, S., 2016. P- and S-wave delays caused by thermal plumes. Geophys. J. Int. 206 (2), 1169–1178.
Matsukage, K.N., Jing, Z., Karato, S.I., 2005. Density of hydrous silicate melt at the conditions of Earth's deep upper mantle. Nature 438 (7067), 488–491.
Morgan, W.J., 1971. Convection plumes in the lower mantle. Nature 230 (5288), 42–43.
Ohtani, E., 2020. The role of water in Earth's mantle. Nat. Sci. Rev. 7, 224–232.
Plomerová, J., Achauer, U., Babuška, V., Vecsey, L., BOHEMA Working Group, 2007. Upper mantle beneath the Eger Rift (Central Europe): plume or asthenosphere upwelling? Geophys. J. Int. 169 (2), 675–682.
Richard, G.C., Bercovici, D., 2009. Water-induced convection in the Earth's mantle transition zone. J. Geophys. Res., Solid Earth 114 (B1), B01205.
Ritsema, J., van Heijst, H.J., Woodhouse, J.H., 1999. Complex shear wave velocity structure imaged beneath Africa and Iceland. Science 286 (5446), 1925–1928.
Ritter, J.R.R., 2005. Small-scale mantle plumes: imaging and geodynamic aspects. In: Wenzel, F. (Ed.), Perspectives in Modern Seismology. Springer, pp. 69–94.
Ritter, J.R., Jordan, M., Christensen, U.R., Achauer, U., 2001. A mantle plume below the Eifel volcanic fields, Germany. Earth Planet. Sci. Lett. 186 (1), 7–14.
Rosenberg, C.L., Handy, M.R., 2005. Experimental deformation of partially melted granite revisited: implications for the continental crust. J. Metamorph. Geol. 23 (1), 19–28.
Safonova, I., Maruyama, S., Litasov, K., 2015. Generation of hydrous-carbonated plumes in the mantle transition zone linked to tectonic erosion and subduction. Tectonophysics 662, 454–471.
Saria, E., Calais, E., Stamps, D.S., Delvaux, D., Hartnady, C.J.H., 2014. Present-day kinematics of the East African Rift. J. Geophys. Res., Solid Earth 119 (4), 3584–3600.
Schuberth, B.S., Bunge, H.P., Ritsema, J., 2009. Tomographic filtering of high-resolution mantle circulation models: can seismic heterogeneity be explained by temperature alone? Geochem. Geophys. Geosyst. 10 (5), Q05W03.
Sleep, N.H., 1996. Lateral flow of hot plume material ponded at sublithospheric depths. J. Geophys. Res., Solid Earth 101 (B12), 28065–28083.
Sobolev, A.V., et al., 2007. The amount of recycled crust in sources of mantle-derived melts. Science 316 (5823), 412–417.
Sobolev, S.V., Zeyen, H., Granet, M., Achauer, U., Bauer, C., Werling, F., Altherr, R., Fuchs, K., 1997. Upper mantle temperatures and lithosphere-asthenosphere system beneath the French Massif Central constrained by seismic, gravity, petrologic and thermal observations. Tectonophysics 275 (1–3), 143–164.
Sobolev, S.V., et al., 2011. Linking mantle plumes, large igneous provinces and environmental catastrophes. Nature 477 (7364), 312–316.
Stern, T., Lamb, S., Moore, J.D., Okaya, D., Hochmuth, K., 2020. High mantle seismic P-wave speeds as a signature for gravitational spreading of superplumes. Sci. Adv. 6 (22), eaba7118.
Tang, Y., et al., 2014. Changbaishan volcanism in northeast China linked to subduction-induced mantle upwelling. Nat. Geosci. 7 (6), 470–475.
Thompson, R.N., Gibson, S.A., 2000. Transient high temperatures in mantle plume heads inferred from magnesian olivines in Phanerozoic picrites. Nature 407 (6803), 502–506.
Tian, Y., Zhu, H., Zhao, D., Liu, C., Feng, X., Liu, T., Ma, J., 2016. Mantle transition zone structure beneath the Changbai volcano: insight into deep slab dehydration and hot upwelling near the 410 km discontinuity. J. Geophys. Res., Solid Earth 121 (8), 5794–5808.
Ueda, K., Gerya, T., Sobolev, S.V., 2008. Subduction initiation by thermal–chemical plumes: numerical studies. Phys. Earth Planet. Inter. 171 (1–4), 296–312.
Wang, W., Walter, M.J., Peng, Y., Redfern, S., Wu, Z., 2019. Constraining olivine abundance and water content of the mantle at the 410-km discontinuity from the elasticity of olivine and wadsleyite. Earth Planet. Sci. Lett. 519, 1–11.
Xia, S., Zhao, D., Sun, J., Huang, H., 2016. Teleseismic imaging of the mantle beneath southernmost China: new insights into the Hainan plume. Gondwana Res. 36, 46–56.
Zhao, D., 2009. Multiscale seismic tomography and mantle dynamics. Gondwana Res. 15 (3–4), 297–323.
Zhao, D., Lei, J., Inoue, T., Yamada, A., Gao, S.S., 2006. Deep structure and origin of the Baikal rift zone. Earth Planet. Sci. Lett. 243 (3–4), 681–691.
Zhao, D., Tian, Y., Lei, J., Liu, L., Zheng, S., 2009. Seismic image and origin of the Changbai intraplate volcano in East Asia: role of big mantle wedge above the stagnant Pacific slab. Phys. Earth Planet. Inter. 173 (3–4), 197–206.
Zhao, D., Yu, S., Ohtani, E., 2011. East Asia: seismotectonics, magmatism and mantle dynamics. J. Asian Earth Sci. 40 (3), 689–709.
Zhou, W.Y., Hao, M., Zhang, J.S., Chen, B., Wang, R., Schmandt, B., 2022. Constraining composition and temperature variations in the mantle transition zone. Nat. Commun. 13 (1), 1094.
Ziegler, P.A., Dèzes, P., 2007. Cenozoic uplift of Variscan Massifs in the Alpine foreland: timing and controlling mechanisms. Glob. Planet. Change 58 (1–4), 237–269.

References (Appendix)

Bangerth, W., Dannberg, J., Fraters, M., Gassmoeller, R., Glerum, A., Heister, T., Myhill, B., Naliboff, J., 2021. ASPECT: Advanced Solver for Problems in Earth's ConvecTion. User Manual. p. 638.
Billen, M., Hirth, G., 2007. Rheology control on slab dynamics. Geochem. Geophys. Geosyst. 8 (8), 2007Q08012.
Burov, E.B., 2011. Rheology and strength of the lithosphere. Mar. Pet. Geol. 28 (8), 1402–1443.
Carmichael, R., 2017. Handbook of Physical Properties of Rocks (1982). Volume II. CRC Press Revivals, CRC Press.

Clauser, C., Huenges, E., 1995. Thermal conductivity of rocks and minerals. In: Ahrens, T. (Ed.), Rock Physics and Phase Relations. A Handbook of Physical Constants. AGU Reference Shelf 3. American Geophysical, Union, Washington DC, pp. 105–126.

Gerya, T., 2019. Introduction to Numerical Geodynamic Modelling, 2nd edition. Cambridge University Press, p. 471.

Hirth, G., Kohlstedt, D.L., 1995. Experimental constraints on the dynamics of the partially Molten upper mantle: deformation in the diffusion creep regime. J. Geophys. Res., Solid Earth 100 (B2), 1981–2001.

Hirth, G., Kohlstedt, D., 2004. Rheology of the upper mantle and the mantle wedge: a view from the experimentalists. In: Eiler, J. (Ed.), Inside the Subduction Factory. Am. Geophys. Union, Washington, DC, pp. 83–105.

Koptev, A., Beniest, A., Gerya, T., Ehlers, T.A., Jolivet, L., Leroy, S., 2019. Plume-induced breakup of a subducting plate: microcontinent formation without cessation of the subduction process. Geophys. Res. Lett. 46 (7), 3663–3675.

Ranalli, G., 1995. Rheology of the Earth, 2nd edition. Chapman and Hall, p. 413.

Shelton, G.L., Tullis, J., Tullis, T., 1981. Experimental high temperature and high-pressure faults. Geophys. Res. Lett. 8 (1), 55–58.

Thieulot, C., 2011. FANTOM: two- and three-dimensional numerical modelling of creeping flows for the solution of geological problems. Phys. Earth Planet. Inter. 188 (1–2), 47–68.